

This is an Open Access document downloaded from ORCA, Cardiff University's institutional repository: <https://orca.cardiff.ac.uk/id/eprint/121122/>

This is the author's version of a work that was submitted to / accepted for publication.

Citation for final published version:

Robinson, Michael, Soe, Shwe, Johnston, Richard, Adams, Rhosslyn, Hanna, Benjamin, Burek, Roy, McShane, Graham, Celeghini, Rafael, Alves, Marcilio and Theobald, Peter 2019. Mechanical characterisation of additively manufactured elastomeric structures for variable strain rate applications. *Additive Manufacturing* 27 , -. 10.1016/j.addma.2019.03.022

Publishers page: <http://dx.doi.org/10.1016/j.addma.2019.03.022>

Please note:

Changes made as a result of publishing processes such as copy-editing, formatting and page numbers may not be reflected in this version. For the definitive version of this publication, please refer to the published source. You are advised to consult the publisher's version if you wish to cite this paper.

This version is being made available in accordance with publisher policies. See <http://orca.cf.ac.uk/policies.html> for usage policies. Copyright and moral rights for publications made available in ORCA are retained by the copyright holders.





25 **Abstract**

26

27 Additive manufacturing (AM) enables production of geometrically-complex elastomeric  
28 structures. The elastic recovery and strain-rate dependence of these materials means they  
29 are ideal for use in dynamic, repetitive mechanical loading. Their process-dependence, and  
30 the frequent emergence of new AM elastomers, commonly necessitates full material  
31 characterisation; however, accessing specialised equipment means this is often a time-  
32 consuming and expensive process. This work presents an innovative equi-biaxial rig that  
33 enables full characterisation via just a conventional material testing machine (supplementing  
34 uni-axial tension and planar tension tests). Combined with stress relaxation data, this  
35 provides a novel route for hyperelastic material modelling with viscoelastic components.  
36 This approach was validated by recording the force-displacement and deformation histories  
37 from finite element modelling a honeycomb structure. These data compared favourably to  
38 experimental quasistatic and dynamic compression testing, validating this novel and  
39 convenient route for characterising complex elastomeric materials. Supported by data  
40 describing the potential for high build-quality production using an AM process with low  
41 barriers to entry, this study should serve to encourage greater exploitation of this emerging  
42 manufacturing process for fabricating elastomeric structures within industrial communities.

43

44 **Keywords**

45 *Elastomeric Polymer Characterisation; Hyperelastic; High strain-rate FEA analysis; Cellular*  
46 *Structures; Viscoelastic*

47

48 **1. Introduction**

49

50 Thermoplastic elastomers (TPEs) are co-polymeric materials that exhibit both thermoplastic  
51 and elastomeric properties, with their functional advantages meaning they are used across a  
52 broad range of applications. Tooling costs associated with traditional manufacturing  
53 methods typically constrains TPE production to high volume components only, limiting  
54 opportunities to lever a performance advantage. The emergence of additive manufacturing  
55 (AM), with unrivalled design freedom and the economic-viability of one-off production,  
56 provides new opportunities to employ TPEs in environments demanding low-volume, high-  
57 performance, or both.

58

59 Finite element analysis (FEA) simulations are well-established in the design, testing and  
60 evaluation of new and novel applications. Emerging techniques including topology  
61 optimisation and cellular lattice generation have supplemented this process, guiding  
62 designers with an over-riding objective function that prescribes the ultimate mechanical  
63 performance [1, 2]. These approaches are now being used in a series of, predominantly  
64 metal-based, weight-sensitive applications [3, 4].

65

66 The success of optimisation techniques is inherently governed by the accuracy of the  
67 material behaviour defined within the simulation. Where the analytical descriptor of a  
68 material's behaviour correlates poorly with its physical performance, the simulation will likely  
69 deliver an inaccurate solution. TPEs, which exhibit a hyper-elastic (HE) response, can be  
70 particularly challenging to characterise due to phenomena such as the Mullin's effect [5],  
71 where stress-softening occurs based on the previous level of strain experienced by the  
72 material. This results in the material's primary response (i.e. that to the first loading) differing  
73 from that of subsequent loading cycles (i.e. the stabilised response). Determining if one, or

74 both, of these responses are of importance to an application, is key to accurately simulating  
75 HE events.

76

77 The non-linear HE response of TPE materials means they cannot be characterised by a  
78 single data-point. Established constitutive models comprise a series of coefficients  
79 associated with strain energy density functions capturing the variation of stress versus strain,  
80 with advanced FEA software enabling the end-user to identify the model with the strongest  
81 correlation to experimental data. Coefficients describing AM-produced materials typically  
82 differ from traditionally manufactured equivalents [6, 7]. Whilst characterisation of AM  
83 metallic structures have now been reported [8, 9], no studies quantify the rate-dependant  
84 behaviour of HE AM material properties when simulating dynamic events. The technical  
85 demands of such characterisation, with laboratories rarely having the requisite facilities  
86 including a stand-alone equi-biaxial testing apparatus [10], risks constraining the  
87 development and uptake of new TPE AM filaments and powders.

88

89 This study describes a novel experimental approach to characterise TPE materials for  
90 applications experiencing strain-rates in excess of quasistatic conditions (referred to as  
91 dynamic strain-rate applications), using solely a commonplace uniaxial testing machine.  
92 Primary, stabilised and rate-dependant responses were captured and then fitted with an  
93 appropriate HE/viscoelastic material model. Computational analysis of an exemplar TPE AM  
94 structure within a dynamic strain-rate environment demonstrates both the validity of this  
95 characterisation process, and the potential to enable high-performance designs.

96 **2. Materials and Methods**

97

98 Uniaxial, equi-biaxial, and planar tension data was collected to define the HE behaviour, for  
99 both primary and stabilised responses. Rate-dependant behaviour was defined by stress  
100 relaxation data. For uniaxial, equi-biaxial and planar tests, strain in the gauge area was  
101 measured using non-contact video-extensometry (iMetrum CAM028, UK). All stresses and  
102 strains are reported as nominal (i.e. engineering) data.

103

104 **2.1. Materials**

105

106 *Table 1. Printing parameters used for this study*

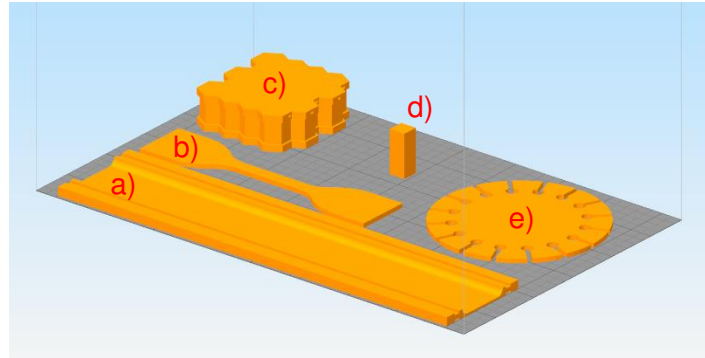
Nozzle Diameter	0.4 mm	Extrusion Multiplier	1.4
Print speed	2000 mm/min	Layer Height	100 µm
Bed Temperature	40 °C	Active cooling	Yes
Extruder Temperature	210 °C	Infill extrusion width	125%

107

108 SOLIDWORKS (Dassault Systems, France) was used to design coupons for each test  
109 method that were manufactured in NinjaFlex (NinjaTek, US), a readily available TPE filament  
110 selected as an exemplar AM material. A fused filament fabrication printer was used (2017  
111 Flashforge Creator Pro printer), retrofitted with high-specification extrusion control (Diabase  
112 Engineering, USA) and using processing parameters tuned to achieve a high extrusion  
113 density. Simplify3D (Simplify3D, US) was used to define print settings and slice the .STL  
114 files for printing. The common rectilinear pattern was adopted for in-filling the parts and X-  
115 ray microscopy (XRM)/microcomputed tomography (µCT) was used to confirm successful  
116 fusing of the infill extrudate. Infill was set to 100% and the extrusion settings tuned to ensure  
117 fusing of the extrudate, allowing confidence that the infill pattern would have minimal effect

118 on experimental results. A honeycomb was also designed and manufactured for use as a  
119 case study to demonstrate the validity of this novel characterisation methodology, with part  
120 quality assessed via  $\mu$ CT. Print orientation is shown in Figure 1.

121



122 *Figure 1. Test part build orientations. a) Planar, b) Uniaxial, c) Honeycomb geometry, d)*  
123 *Cuboid for  $\mu$ CT Scanning, e) Equi-biaxial*

124

## 125 2.2. Methods

126

127 A preliminary simulation was undertaken to establish the minimum/maximum strains  
128 experienced during the loading of the honeycomb structure. This allowed identification of  
129 the appropriate cycled strain during mechanical testing, used to describe the stabilised  
130 response of the TPE material. A linear elastic model [11] was applied to the honeycomb  
131 structure, which was compressed within ABAQUS to densification. The recorded strain was  
132 approximately  $\pm 0.3$  throughout the simulated densification of the honeycomb (to  $\sim 60\%$  of  
133 its original height). This guided the adoption of an upper strain threshold of 0.4 for  
134 mechanical testing.

135 During the preliminary simulation, a mesh sensitivity study was undertaken. Varying the  
136 element size from one-quarter, to twice, the wall thickness, achieved near-identical force-

137 displacement curves and little variation in predicted energies, which is consistent with other  
138 studies investigating dynamic compression of cellular structures [12].

139 Five samples were manufactured for each test setup described in section 2.2.1.

140

### 141 *2.2.1. Mechanical Testing*

142

#### 143 *Uniaxial (Tension) Testing*

144

145 Testing was performed using an electromechanical uniaxial testing machine (Zwick Z50,  
146 Germany), following ISO 37 [13] with a reduced crosshead speed (100mm/min), to minimise  
147 strain rate sensitivity. Test coupons were designed and fabricated as per tensile testing  
148 specimen type 1 [13]. Investigation was performed over cyclical loading to 0.4 strain.

149

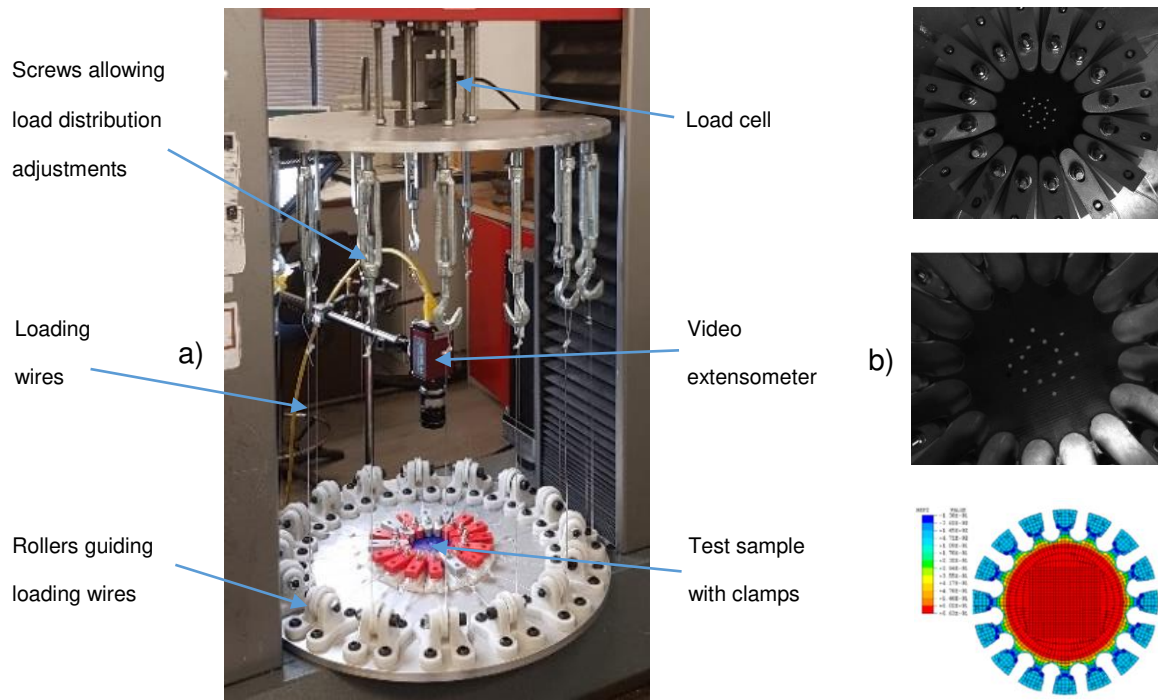
#### 150 *Equi-Biaxial (Tension) Testing*

151

152 An equi-biaxial test apparatus was designed and built in-house, to enable multi-axial data  
153 generation from a single uniaxial testing machine. Novel test coupons were designed and  
154 manufactured, including 16 clamping tabs that enabled uniform application of a multi-axial  
155 load, generating equi-biaxial strain in the coupon centre (Figure 2 a & b). These test  
156 specimens have been shown to be appropriate for equi-biaxial testing [10], with FE analysis  
157 showing little influence of geometry on the state of stress in the central gauge section.  
158 Machine parameters and cycled strain were consistent with the uniaxial setup.

159





160 *Figure 2: a) Equi-biaxial test rig, b) Stretching of Equi-biaxial sample in this study, and FEA*  
 161 *validation of sample performed by Day, J. (reproduced from [10])*

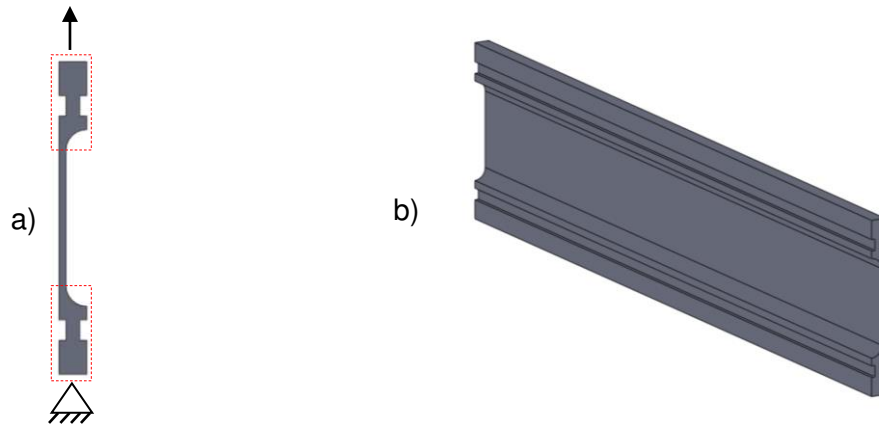
162

163 *Planar (Tension) Testing*

164 Shear data is valuable when modelling hyperelastic materials, which is derived from planar  
 165 tension testing [14, 15]. Novel planar coupons were designed to include ridges, which  
 166 improved gripping and ensured load distribution into the test gauge area (Figure 3 a & b).  
 167 Machine parameters and cycled strain were again consistent with the uniaxial setup.

168

169



170 *Figure 3: a) Side profile highlighting ridges/added geometry on planar sample, b) 3D*  
 171 *visualisation of planar sample*

172

173 *Stress Relaxation Testing*

174

175 The uniaxial test geometry was used to measure stress relaxation, performed at the  
 176 maximum available cross-head speed (600mm/min), to a strain of 0.4 and followed by a  
 177 100s relaxation period. Stress relaxation experiments cannot achieve an instantaneous step  
 178 input and will always include an initial loading ramp, as well as inertial effects from the test  
 179 equipment loading. The user must compensate for these effects when analysing the data,  
 180 by back-calculating to a theoretical instantaneous load point, as has been performed here.

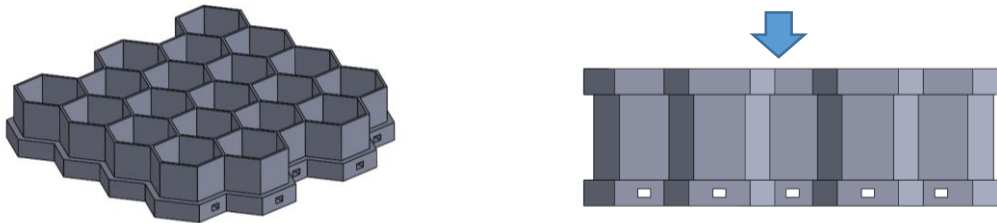
181 *Mechanical Testing of Exemplar TPE AM Honeycomb*

182

183 A NinjaFlex hexagonal honeycomb was designed and manufactured to validate the above  
 184 characterisation process and to demonstrate the potential of AM TPEs to produce structures  
 185 for high performance applications. The honeycomb structure consisted of a 4x5 unit cell,  
 186 with each cell having a side length of 5.8mm, 10mm height and 0.4mm wall thickness. Two  
 187 3mm thick solid sections were designed onto the upper and lower surfaces of the  
 188 honeycomb, to achieve well-defined boundary conditions. Exhaust channels (1mm

189 diameter) were designed in to the lower solid section, enabling release of air trapped within  
190 the honeycomb cavities during compression and impact testing.

191



192 *Figure 4. a) sectioned view of the honeycomb part, b) indication of load direction on part*

193

194 The honeycomb structure was cyclically compressed to densification (~60% of its original  
195 height) at 100mm/min (i.e. quasistatically). Industrial-strength adhesive tape (Tesa 64621)  
196 was used to adhere the solid sections to the compression platens, ensuring consistent  
197 boundary conditions. Dynamic testing was then performed to evaluate the relative  
198 performance of the TPE AM honeycomb in a dynamic strain rate environment. A guided  
199 drop tower (Instron 9250HV, US) was used to strike the honeycomb test geometry with a  
200 3.53kg impactor at 1.4 m/s. This velocity ensured the honeycomb compressed to >60% of  
201 its overall height. An in-line accelerometer (Kistler 8715A, Switzerland) was used to record  
202 the acceleration-time pulse. Boundary conditions were defined by the lower solid section of  
203 the honeycomb geometry being adhered to the anvil, and the impactor and upper solid  
204 section of the honeycomb being covered with sandpaper. The impactor was released from  
205 0.01m, allowing dynamic compression of the honeycomb to 60% of its original height.  
206 Acceleration-time pulses were converted using standard formulae into force-displacement  
207 and displacement-time data.

208

209 *Statistical Analysis*

210

211 Results of each test method are displayed as a mean value, with error bars representing the  
212 standard deviation (SD). All testing was performed through 5 cycles/impacts, to account for  
213 stress softening behaviour in the material, which decreased markedly after the second cycle  
214 and was cycled a further three times to ensure a stabilised response.

215

216 *2.2.2. Computational Analysis and Validation*

217

218 ABAQUS 6.14 (Dassault Systems, France) was used first to curve-fit an appropriate material  
219 model to the primary and secondary responses (for dynamic simulations the viscoelastic  
220 component was added to these material models), before enabling analysis of the primary  
221 and stabilised performance of an exemplar honeycomb structure. An appropriate material  
222 model was then selected based on the closest correlation with the test data. Explicit  
223 Dynamic Analysis was used and, in addition to any other boundary conditions/interactions  
224 defined in the simulation, a global frictionless contact was defined to prevent self-penetration  
225 of the honeycomb. Incompressibility was assumed (i.e. Poisson's ratio = 0.475, as this is  
226 the maximum allowable in ABAQUS) and enhanced hourglass control implemented. Hyper-  
227 elastic material models were fitted separately to primary and stabilised datasets. Ogden 1<sup>st</sup>  
228 to 6<sup>th</sup> order, Polynomial 1<sup>st</sup> and 2<sup>nd</sup> order and Reduced Polynomial 1<sup>st</sup> to 6<sup>th</sup> order models  
229 were investigated for each state. The viscoelastic component of the material model was  
230 defined using normalised stress relaxation data, fitted by ABAQUS to a Prony series with  
231 0.001 minimum allowable root-mean-square error. A continuum element hex-dominated  
232 mesh was proliferated throughout with a seed equal to the measured average wall thickness  
233 of the honeycomb (0.45 mm); however, the 3mm thick upper and lower sections of the test

234 part were partitioned and given a larger (default) edge seed of 0.72 mm, to reduce the  
235 computational cost.

236

237 Due to the honeycomb walls being the same thickness as the extrusion nozzle, it was  
238 expected the manufactured wall thickness would increase. Average wall thickness was  
239 measured by  $\mu$ CT and used to update the honeycomb CAD for ABAQUS simulations. This  
240 ensured identical geometry of the simulated and mechanically tested parts.

241

242 Quasistatic compression was computationally modelled with the honeycomb component  
243 sandwiched between two rigid flat plates. The upper plate was tied to the upper solid  
244 section of the honeycomb and prescribed a deflection of 0.6mm, over 1s. The lower plate  
245 was fixed in space and tied to the lower honeycomb face. Viscoelastic material properties  
246 were not included, whilst a mass scaling of 20 considerably reduced simulation time with  
247 minimal influence on accuracy. The force-time and displacement-time histories were  
248 extracted from a reference node at the centre of the upper rigid plate, enabling direct  
249 comparison with mechanical testing results.

250

251 For simulated validation of the impact tests, the honeycomb was again sandwiched between  
252 two rigid flat plates in ABAQUS. The upper plate was now assigned a 3.53kg point mass  
253 and prescribed a pre-impact velocity observed during experimentation. A sliding frictional  
254 coefficient of 1 was defined between the upper honeycomb surface and adjacent plate, to  
255 represent a sandpaper-sandpaper contact. The lower honeycomb face was tied to the  
256 bottom plate, which was fixed in space. The acceleration-time and displacement-time  
257 histories were extracted from a reference node at the centre of the upper rigid plate, for  
258 comparison with mechanical testing results. Acceleration-time was converted to force-time  
259 using Newton's second law of motion.

### 2.2.3. X-ray Microscopy (XRM)/Microcomputed Tomography Scanning ( $\mu$ CT)

261

262 Porosity analysis was performed using a nominal cuboid structure (7.5 x 7.5 x 20 mm)  
263 manufactured from NinjaFlex and by adopting the established processing parameters.  
264 Analysis was performed via XRM using a lab-based Zeiss Xradia 520 (Carl Zeiss XRM,  
265 Pleasanton, CA, USA) X-ray Microscope, using a CCD detector system with scintillator-  
266 coupled visible light optics and tungsten transmission target. To achieve a higher resolution  
267 over the entire part height, the specimen was imaged along its 20 mm length at high  
268 resolution, using an overlap-scan and stitching procedure including five individual scans,  
269 with 15% overlap between each scan. An X-ray tube voltage of 60 kV and a tube current of  
270 80  $\mu$ A were used, with an exposure of 1000 ms and a total of 3201 projections. An objective  
271 lens giving an optical magnification of 0.4 was selected with binning set to 2, producing an  
272 isotropic voxel (3-D pixel) sizes in the range 11.862  $\mu$ m. The tomograms were reconstructed  
273 from 2-D projections using a Zeiss commercial software package (XMReconstructor, Carl  
274 Zeiss), a cone-beam reconstruction algorithm based on filtered back-projection.  
275 XMReconstructor was also used to produce 2-D grey scale slices for subsequent analysis.  
276 A threshold size of 2 voxels was implemented, reflecting the boundary between pore (gas)  
277 and material of the smallest pores. Excluding data below this threshold avoids inaccurately  
278 including smaller pores during the segmentation process.

279

280 The honeycomb sample was imaged using a lab-based Nikon XT H225 microfocus X-ray  
281 microtomography ( $\mu$ CT) system, with a 1.3 Megapixel Varian PaxScan 2520 amorphous  
282 silicon flat panel digital X-ray imager, in reflection mode with a molybdenum target. An X-ray  
283 tube voltage of 60 kV and a tube current of 130  $\mu$ A were used, with an exposure of 1000 ms  
284 and a total of 3015 projections, with a voxel (3-D pixel) size of 15.05  $\mu$ m. The tomograms  
285 were reconstructed from 2-D projections using a Nikon commercial software package  
286 (CTPro version 3.0, Nikon Metrology), a cone-beam reconstruction algorithm based on

287 filtered back-projection. The commercial software VGStudio Max 2.1.5 was used to view the  
288 reconstructed data and produce 2-D grey scale slices in TIFF format. These were imported  
289 into Avizo Software (ThermoFisher Scientific, Waltham, MA, USA), where post-processing  
290 including reorientation, binarization and segmentation allowed extraction of pore size and  
291 volume. Honeycomb average wall thickness was measured using Vernier callipers, as well  
292 as digitally via the  $\mu$ CT data using SOLIDWORKS (Dassault Systems, France) and used to  
293 update the equivalent CAD/FEA model used for computational simulation.

294

295 **3. Results**

296

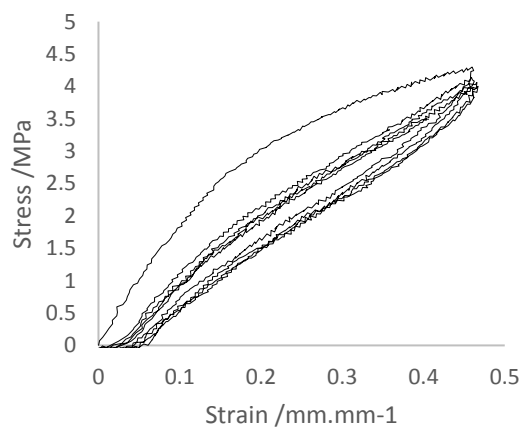
297 **3.1. Mechanical Testing**

298

299 The test results showed that the equi-biaxial response generated a higher stress than the  
300 planar response, which was greater than the uniaxial response, at any given strain (Figure  
301 6). This trend was consistent when considering both the primary and stabilised response.

302 Stress and strain for uniaxial and planar testing are presented based on the direction of the  
303 loading.

304



305 *Figure 5. cyclic behaviour of NinjaFlex under uniaxial loading*

306

307 **3.1.1. Primary HE response**

308

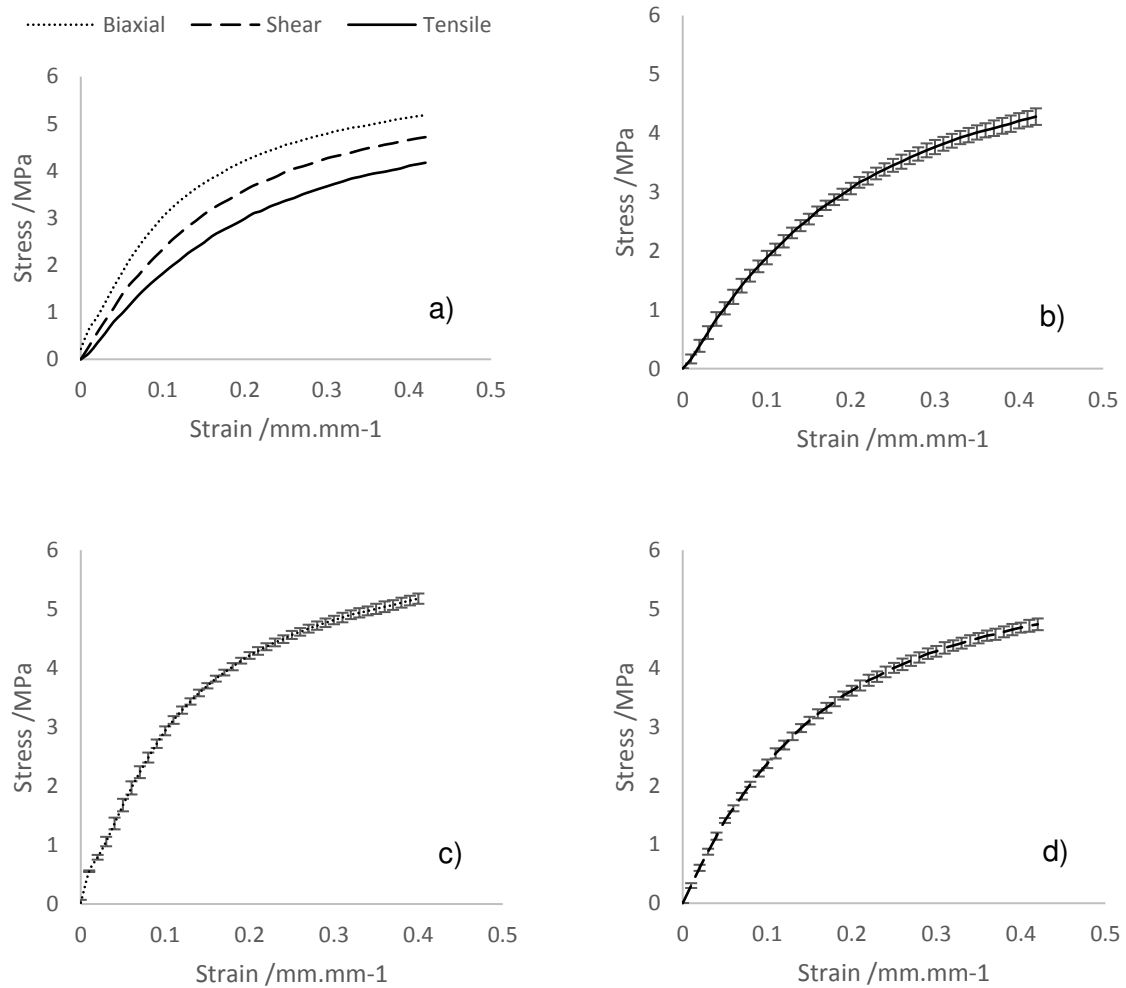
309 All datasets demonstrated non-linear behaviour typical of elastomeric materials. Uniaxial  
310 testing gave an average initial modulus of 18.2MPa, when considering strains from 0 to 0.1.

311 The average initial planar modulus was 28% greater than uniaxial and the average initial  
312 equi-biaxial modulus 66% greater. At a strain of 0.4, uniaxial stress was 4.11 MPa, planar



313 stress was 4.66 MPa and equi-biaxial stress was 5.13MPa. The full data curves showing the  
314 average mechanical test data are displayed in Figure 6.

315



316 *Figure 6 Mechanical testing for average primary response of: a) Combined data sets, b)*  
317 *Uniaxial only, c) Equi-biaxial only, d) Planar only. Error bars = SD*

318

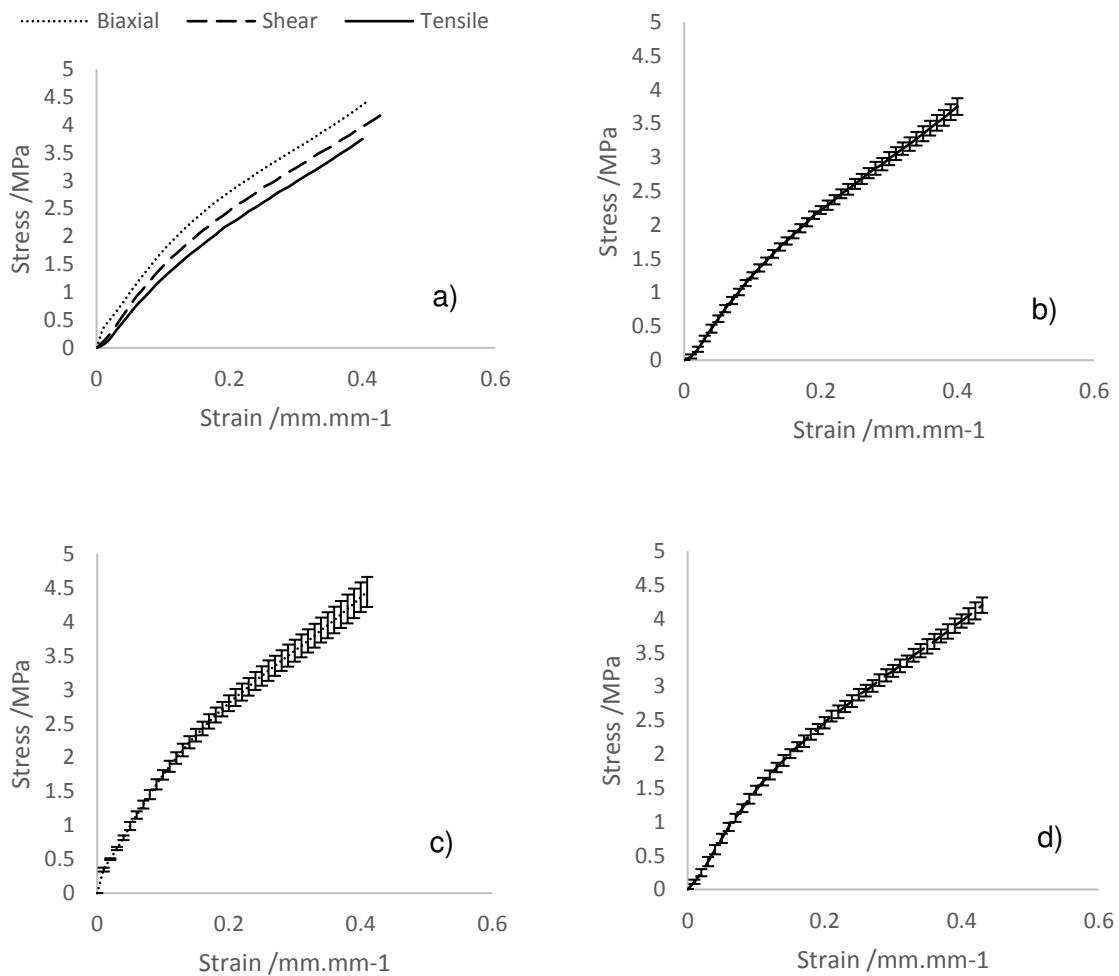
### 319 *3.1.2. Stabilised HE response*

320

321 The planar data trend was closer to the uniaxial, than equi-biaxial, response. Uniaxial  
322 testing gave an average initial modulus of 12.5MPa, when considering strains from 0 to 0.1.

323 The average initial planar modulus was 18% higher than uniaxial, with the average initial  
 324 equi-biaxial modulus 39% higher. At a strain of 0.4, uniaxial stress was 3.75 MPa, planar  
 325 stress was 3.97 MPa and equi-biaxial stress was 4.36 MPa. Variance between the 5 test  
 326 samples for each stress state of the stabilised response was minimal, though larger than the  
 327 primary response data (Figure 7).

328



329 Figure 7 Mechanical testing for the average stabilised response of: a) Combined data sets,  
 330 b) Uniaxial only, c) Equi-biaxial only, d) Planar only. Error bars = SD

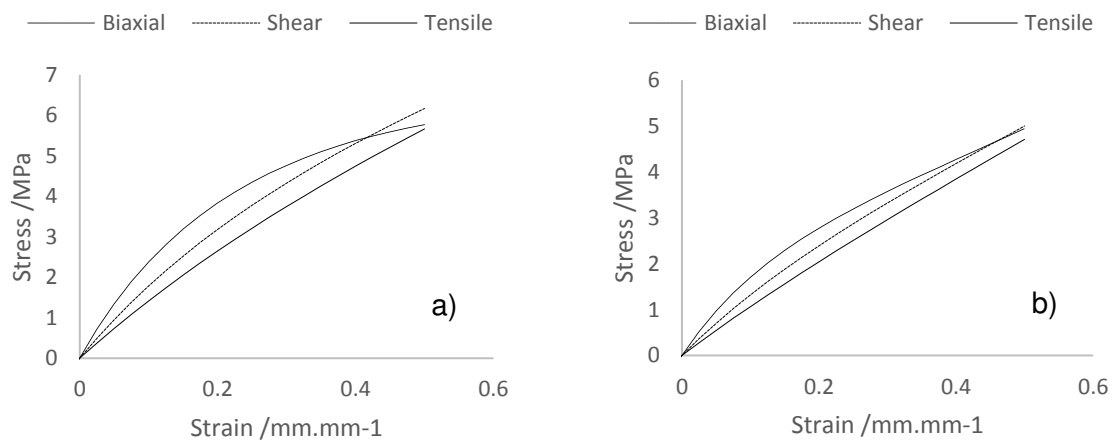
331

332 3.2. Curve-fitting

333

334 The ABAQUS-based curve fitting procedure for the primary and stabilised responses are  
335 presented in Figure 8. The Mooney-Rivlin model provided the most appropriate fit to the  
336 primary response, whilst the 2<sup>nd</sup> order Ogden model provided the best fit for the stabilised  
337 response.

338



339 *Figure 8 Graphs showing combined fit for: a) Primary response, b) Stabilised response*

340

341 The coefficients for the primary and stabilised responses material models are presented in  
342 Table 2 and Table 3. These models are mathematically stable, both fitting well to  
343 experimental extension data and sensibly predicting the compressive behaviour, for the  
344 positive and negative strain (+/- 0.3) estimated in the preliminary unit cell investigation  
345 (Section 2.2.1). It should be noted that outside of the predicted strain range both models  
346 become increasingly inaccurate.

347

348 *Table 2 Primary response – Mooney-Rivlin material model coefficients*

$C10$ /MPa	$C01$ /MPa
2.93	0.363

349

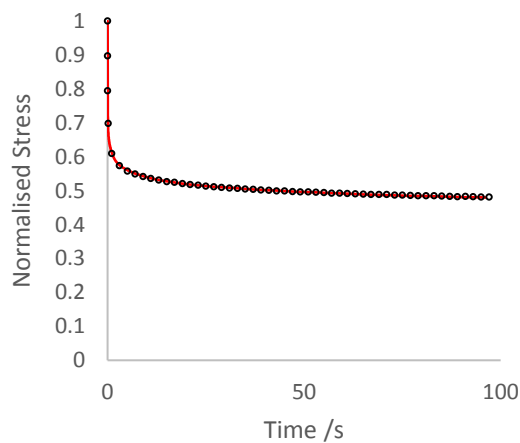
350 *Table 3 Stabilised response – 2<sup>nd</sup> order Ogden material model coefficients*

	$\mu1$ /MPa	$\alpha1$
1	12.2	1.87
2	8.41	1.19

351

352 Due to the specified low root mean square (RMS) error (0.001), the Prony series were  
 353 calibrated closely to the experimental data (Figure 9). Examining the experimental data  
 354 trend enables estimation of a long-term normalised modulus between 0.4 - 0.5. The Prony  
 355 coefficients that define the curve presented in Figure 9 are quantified in Table 4.

356



357 *Figure 9 Normalised uniaxial stress relaxation data, with Prony series curve fit*

358

359 *Table 4 Viscoelasticity Prony series*

	<i>G /MPa</i>	<i>K /MPa</i>	<i>tau /s</i>
1	0.196	0.0000	1.27E-03
2	0.129	0.0000	8.30E-02
3	7.67E-02	0.0000	0.894
4	6.03E-02	0.0000	6.51
5	7.10E-02	0.0000	54.6

360

361

362

363

364

365

366

367

368

369

370

371

372

373

374

375

376

377

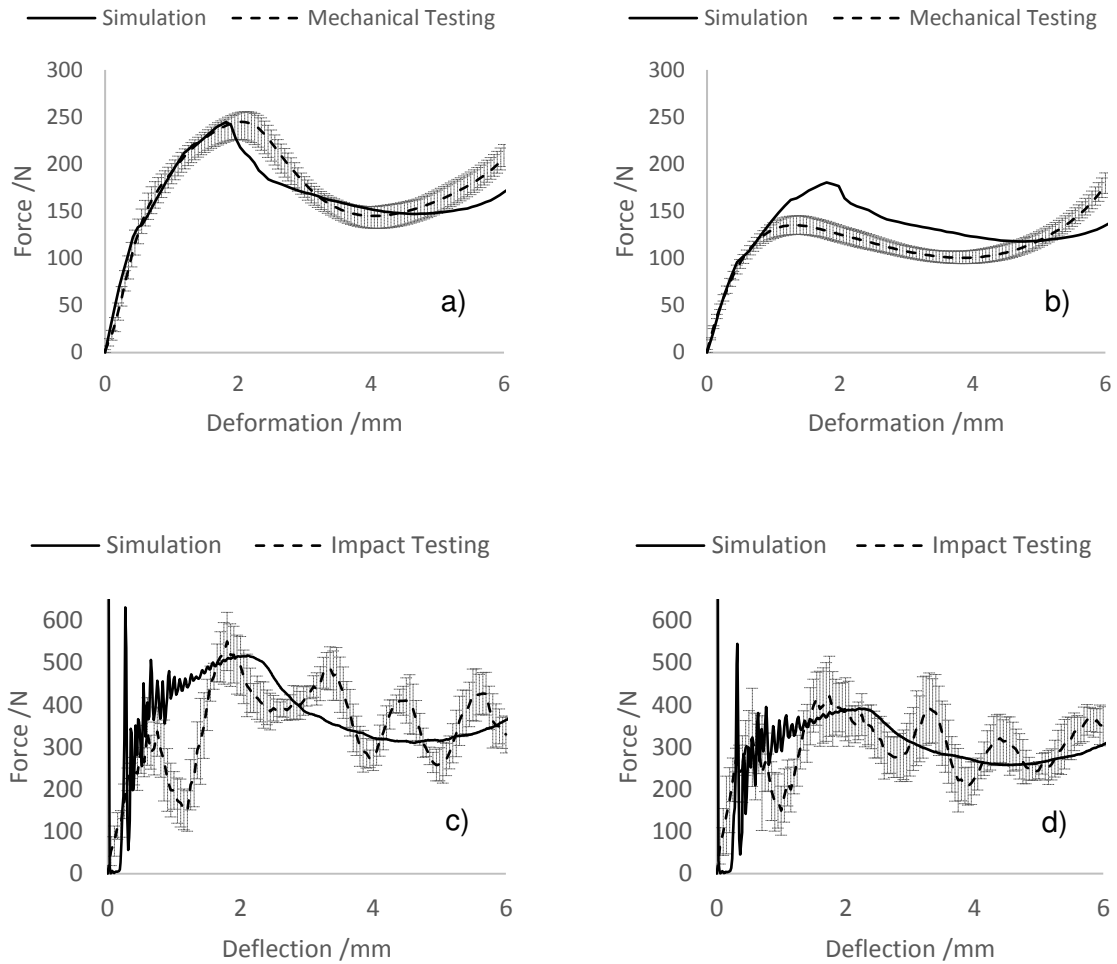
378

379

380

381

382 3.3. Honeycomb testing



383 *Figure 10 Honeycomb validation, plotting mechanical test data alongside related simulations:*

384 *a) Primary quasistatic, b) Stabilised quasistatic, c) Primary impact, d) Stabilised impact.*

385 *Error bars = SD*

386

387 *Quasistatic Honeycomb Compression*

388

389 The plateau region varies between experimental and simulation results, influencing the

390 energy absorbed by each structure prior to densification (Table 5). For the simulated

391 primary response, agreement exists between the experimental and simulation peak forces

392 and absorbed energy; however, an increase in peak displacement of 11% was observed in

393 the experimental results. The stabilised energies for the simulated and experimental results  
 394 were within 10% of one another.

395

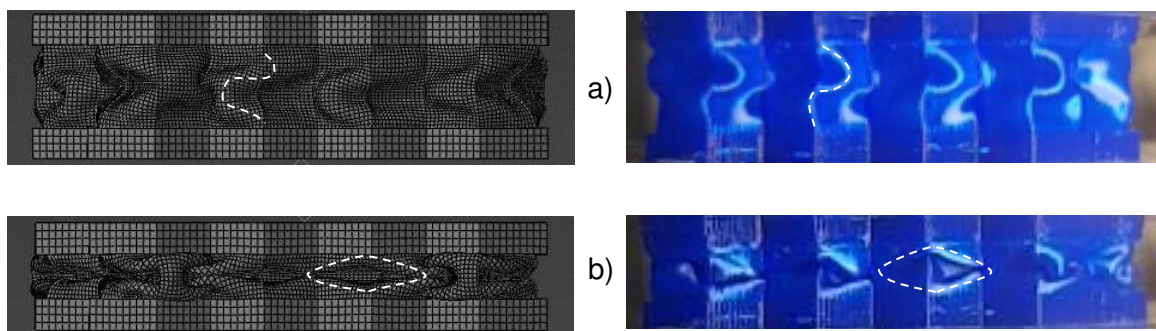
396 *Table 5 Peak quasistatic forces/displacements at commencement of plateau region + energy*  
 397 *absorbed by structure prior to densification*

	<i>Peak force pre- plateau /N</i>	<i>Displacement of peak force /mm</i>	<i>Energy absorbed by 6mm /J</i>
<i>Simulation Primary response</i>	245	1.82	1.00
<i>Mean Experimental Primary response</i>	245	2.05	1.04
<i>Simulation Stabilised response</i>	180	1.80	0.77
<i>Mean Experimental Stabilised response</i>	137	1.25	0.69

398

399 At 2mm, similar s-shaped and arrow-shaped deformation patterns were observed in  
 400 experimental testing and simulation (Figure 11). At greater levels of compression (2 –  
 401 6mm), the structure begins to fold inside itself with elongated diamond-shaped patterns.

402



403 *Figure 11 Comparison of simulated and experimental deformation during quasistatic*  
 404 *compression: a) 2mm, b) 6mm. Note, simulated images have been flipped horizontally to*  
 405 *better highlight the similar deformation patterns.*

407

408 *Data describing the plateau regions is presented in*

409 Table 6. Experimental and simulated peak forces, displacements and energies absorbed  
 410 were all within 10% of one another for the dynamic primary and stabilised responses, except  
 411 the stabilised peak displacement, where the mechanical testing was 30% lower.

412

413 *Table 6 peak forces/displacements at commencement of plateau region + energy absorbed*  
 414 *by structure prior to densification dynamic*

	<i>Peak force pre- plateau /N</i>	<i>Displacement of peak force /mm</i>	<i>Energy absorbed by 6.5mm /J</i>
<i>Simulation Primary response</i>	515	1.97	2.21
<i>Mean Experimental Primary response</i>	550	1.80	2.10
<i>Simulation Stabilised response</i>	391	2.20	1.75
<i>Mean Experimental Stabilised response</i>	420	1.75	1.77

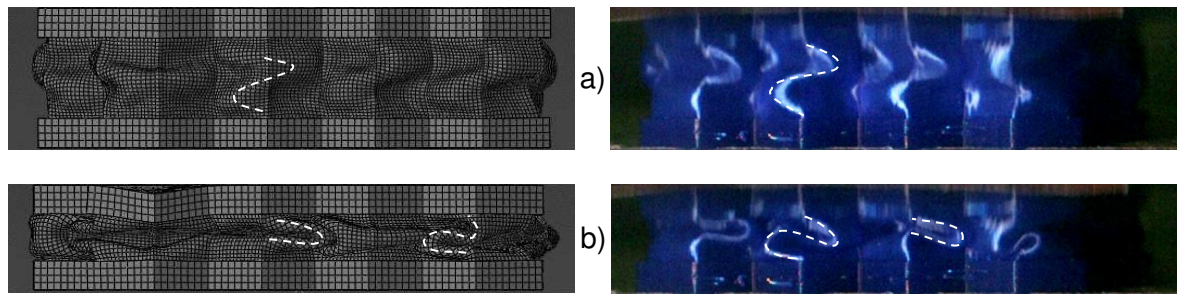
415

416 Distinct s-shaped deformation was identified both in experimental testing and simulation, at  
 417 2mm compression (Figure 12). At 6mm, the experimental testing and simulation  
 418 demonstrated distinctive arrow-shaped and s-shaped deformation patterns; however, the  
 419 simulation also had outer walls folding into the centre of the structure, similar to observations  
 420 during quasistatic compression (Figure 11).

421

422





423 *Figure 12 Comparison of simulated and experimental deformation during impact: a) 2mm, b)*  
 424 *6mm. Note, simulated images have been flipped horizontally to better highlight the similar*  
 425 *deformation patterns.*

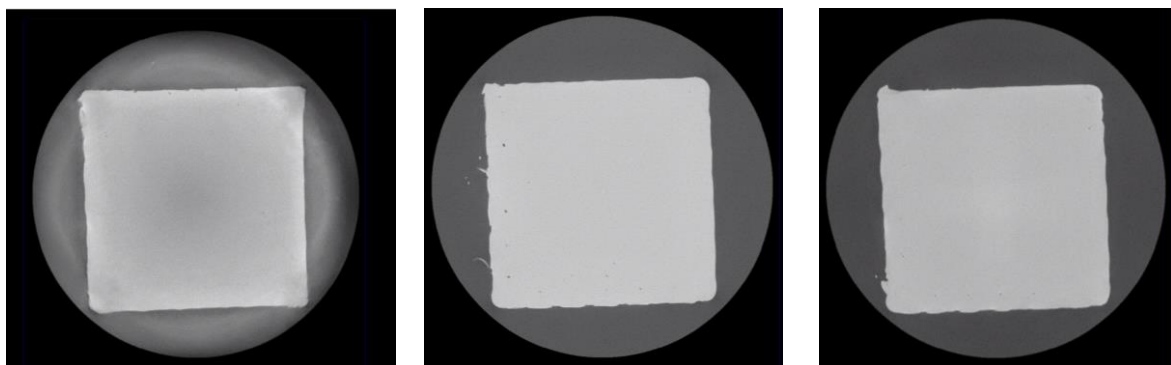
426

### 427 3.4. XRM/μCT Analysis

428

429 μCT scanning demonstrated that manufactured parts were largely homogenous, meaning  
 430 successful fusion of the extruded material (Figure 13). Additionally, the outline bounding the  
 431 internal rectilinear patterning was continuous, with no pores observed throughout its height.

432



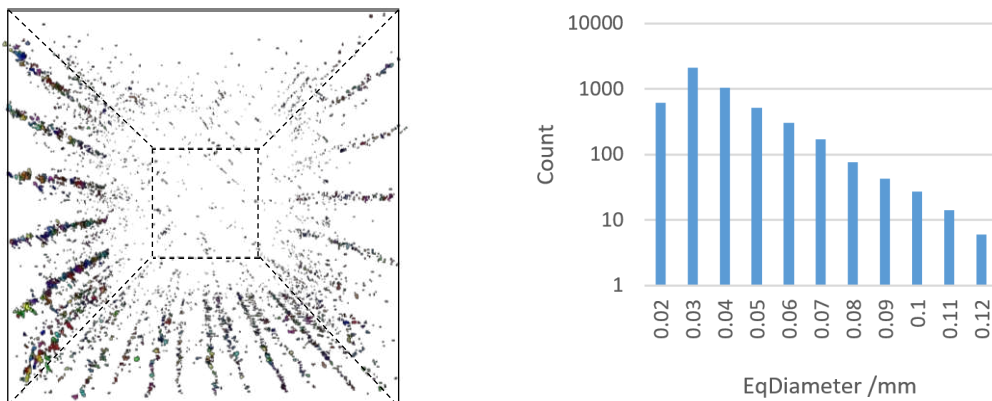
433 *Figure 13 CT scanned cross-sections of cuboid geometry. Left-right: bottom, centre, top*

434

435 When analysing the pores within the scanned cuboid, those of equivalent diameter  $\leq 2$  voxels  
 436 (equivalent to  $23.7 \mu\text{m}$ ) were excluded. This was due to the potential lack of accuracy when  
 437 detecting pore edges of such small pores. Analysis of the remaining pores suggested the

438 cuboid was 99.97% dense, with an average pore size of 38  $\mu\text{m}$  and a max pore size of 119  
 439  $\mu\text{m}$ . Only ~10% of the pores were 60-119  $\mu\text{m}$ , which appeared concentrated between the  
 440 rectilinear fill forming the cuboid centre and the outline forming the perimeter. The  
 441 distribution of the pores within the cuboid and the pore diameter histogram, are presented in  
 442 Figure 14. A one-point perspective view down the length of the cuboid illustrates the pore  
 443 distribution (Figure 14a). The largest pores are located at the boundary of the outline and  
 444 the infill pattern, in lines running the height of the cuboid.

445



446 *Figure 14 a) 3D image of pores within the cuboid structure, with a bounding outline to show*  
 447 *the approximate position of the cuboid exterior, b) histogram showing the effective length of*  
 448 *each pore*

449

450 The  $\mu\text{CT}$  scan and supporting vernier measurements of the honeycomb walls gave an  
 451 average thickness of 0.45mm (versus 0.4mm for the CAD design) with a SD of 0.01 mm.  
 452 The averaged value was used to simulate a part of constant wall thickness within ABAQUS,  
 453 based on the minimal deviation. Some material could be observed drooping as the upper  
 454 surface 'bridged' over the honeycomb cell wall; however, this appeared minimal and did not  
 455 affect adhesion between these two features.

456

457 **4. Discussion**

458

459 The mechanical performance of TPE AM materials are known to vary with processing  
460 parameters, whilst new products regularly enter the market; hence, there is an increasing  
461 need to perform full characterisation, though the requisite equi-biaxial facilities remain  
462 scarce.

463

464 This study has demonstrated success with a novel approach to material characterisation,  
465 validated by the comparable trends achieved when experimentally and computationally  
466 compressing a honeycomb structure. When applying the material models to a multi-strain  
467 rate and state application, a close correlation between predicted and experimental data was  
468 observed (Figure 10). The stress-softening characteristic of the Mullin's effect is evident  
469 when comparing Figure 6 and Figure 7. Even at a relatively low strain (0.4), the initial  
470 stiffness of the primary response is 31% higher than that of the stabilised response, and  
471 15% higher stress at maximum strain. This reinforces the importance of understanding and  
472 selecting the correct material response when simulating TPEs in specific applications. This  
473 study has also highlighted the need to characterise multiple responses for a single material,  
474 with both primary and stabilised responses being required to validate consecutive dynamic  
475 compressions of a honeycomb structure (Figure 10).

476

477 Good correlation was achieved between the HE material models and experimental data  
478 across both the primary ( $r^2 = 0.97$ ) and stabilised ( $r^2 = 0.99$ ) response. Such strong  
479 correlation provided a robust platform to investigate dynamic strain-rate applications. The  
480 low RMS error requirement placed on the stress relaxation data meant that the viscoelastic  
481 portion of the material model closely followed the experimental response. Consequently,

482 these material models accurately simulate NinjaFlex behaviour in dynamic applications of a  
483 similar strain (i.e. +/-0.3).

484

485 Applying the material model to the honeycomb structure achieved strong comparability  
486 between simulation and experimental data. This strong correlation validates this novel  
487 method for TPE characterisation, whilst also demonstrating the potential for use in complex  
488 geometries within dynamic environments. The mechanical response (Figure 10) and  
489 deformation patterns (Figure 11 and Figure 12) demonstrated excellent prediction of a  
490 complex HE buckling event. The quasistatic stabilised experimental and computational  
491 investigations exhibited the weakest correlation. This may be caused by the residual strain  
492 accumulated during stabilising loading cycles which, in combination with the fixed boundary  
493 condition created by the adhesive tape, resulted in a period of tensile loading as the actuator  
494 returned to the datum. Whilst this was noted and appropriately adjusted for during data  
495 analysis, this additional loading regime could have triggered a unique response within the  
496 material, meriting future investigation.

497 The experimental and simulated honeycombs exhibited discrepancies between their  
498 deformation patterns during dynamic loading (Figure 12). Whilst the honeycomb walls  
499 appeared to all form s-shaped profiles during experimental testing, a combination of s-  
500 shaped and inward folding behaviour was observed in the simulated deformation patterns.  
501 This appears to be focussed around the bending of the upper thick section's profile within  
502 the simulation, causing inward folding to occur underneath. AM inherently results in  
503 inconsistent wall thickness, minimal variation was evident and strong correlation existed  
504 between the simulated and experimental stress-strain behaviour; however, such  
505 manufacturing variability could still have influenced the observed deformation patterns.  
506 Additionally, the buckling in the structures is a non-trivial event and, therefore, some  
507 deviation in deformation patterns was expected between the simulated and experimental  
508 behaviour. Structural response can also be influenced by contact behaviour; however, this

509 study investigated pre-densification behaviour and, when running these simulations with a  
510 general frictional contact (as opposed to frictionless), minimal change in stress-strain  
511 behaviour was observed.

512

513 This study assumed linear viscoelasticity and, whilst the use of non-linear viscoelastic  
514 models may help to further fine-tune the prediction of varying strain rate behaviour, this  
515 comes at a substantial computational time cost. In the light of this drawback, the close  
516 correlation of predicted behaviour presented here serves to justify the assumption of linear  
517 viscoelasticity. In the light of mainstream adoption due to low machine costing, fused  
518 filament fabrication (FFF) is considered by many to be a rudimentary/entry level technique.  
519 The potential of FFF to produce high quality components is, however, demonstrated here,  
520 with an excellent cuboid part density of 99.97%. This exceeds previously reported densities  
521 achieved via Selective Laser Sintering (SLS) TPE components (~95%) [16] and is  
522 comparable to injection moulded parts. Accounting for 94% of the cumulative pore volume,  
523 the largest voids (70-119 $\mu$ m) are technically challenging to eliminate in FFF builds and  
524 existed between the rectilinear fill and bounding outline of the cuboid. During tuning of  
525 processing parameters, attempts to reduce these voids included the use of concentric  
526 (instead of rectilinear) fill, increasing extrusion multiplier, and increasing overlap between the  
527 inner rectilinear fill and bounding outline. These methods introduced their own issues such  
528 as the concentric fill generating significant voids in the centre of the part, whilst increasing  
529 overlap/extrusion multiplier resulted in distortion of printing parts. It should be noted that the  
530 threshold size of 20 $\mu$ m was selected to ensure the pores within the entirety of the cuboid  
531 could be captured in a single scan. Whilst this provides a suitable indicator of the porosity of  
532 the part (as the pores circa 70-110 $\mu$ m accounted for 94% of the measured pore volume),  
533 this has the potential to filter out smaller pores that could have an undetermined influence on  
534 material behaviour.

535 It is known that the layer-by-layer AM build process produces component anisotropy, with  
536 this behaviour frequently noted in the literature perpendicular to the layer deposition [17-19].  
537 This behaviour is highly dependent on manufacturing build quality as this logically effects the  
538 inter-layer bonding. As complex printed components can be exposed to different strain  
539 states, potential exists for loadings to be applied parallel and perpendicular to inter-layer  
540 bonding, even if the overall structure is only under compressive loading. Due to the lack of  
541 notable voids, similar deformation patterns/mechanical responses and good correlation  
542 between stress-strain behaviour of the honeycomb structure, no further investigation of  
543 anisotropy was performed in this study. AM manufacture also means that thin some  
544 geometric features comprise only a single track of extruded filament (i.e. as per the entire  
545 honeycomb structure), creating the potential for a different mechanical response than parts  
546 with infill patterning (e.g. test parts used to characterise NinjaFlex). This risk was mitigated  
547 against by using process parameters that achieved minimal voids in the recti-linear fill  
548 pattern, with good correlation evident between the simulated honeycomb response (using  
549 infill patterning characterisation) and the mechanical testing (of single extrudate honeycomb  
550 print).

551 **5. Conclusions**

552

553 This study has achieved a greater understanding of the behaviour of TPE AM materials,  
554 enabling more effective exploitation of this emerging technology. A novel approach to  
555 efficiently and robustly characterise TPE materials has been presented. The importance of  
556 considering strain-softening has also been demonstrated, along with the potential to design  
557 and analyse AM structures for high performance applications. Highlighted findings include:

- 558 • Multi-state strain data to define a material model has been acquired using a standard  
559 uni-axial testing machine.
- 560 • A material model has been fitted to the TPE test data, including viscoelastic effects.  
561 This model is then successfully validated through its application to a case study of a  
562 traditional hexagonal honeycomb at varying strain rate.
- 563 • The level to which the TPE material was strained had significant effects on  
564 subsequent straining of the material, an important consideration when developing  
565 material models for applications involving multiple cycling events.
- 566 • When dynamically compressed, the viscoelastic properties significantly affect the  
567 recorded forces, demonstrating a significant degree of strain-rate dependence.  
568 These strain-rate effects carried over to the manufactured parts, resulting in a  
569 significant increase in recorded force when dynamically compressed, compared to  
570 quasistatic compression.
- 571 • FFF has been used to fabricate TPU components of high homogeneity (material  
572 density of 99.97%), with expected manufacturing considerations spreading material  
573 at the extruder nozzle, resulting in an increased wall thickness.

574

575

576 **6. Acknowledgements**

577

578 M. Robinson was supported by the Knowledge Economy Skills Scholarships 2 (via the  
579 Welsh Government's European Social Fund).

580 The X-ray imaging work was supported by the Advanced Imaging of Materials (AIM) facility  
581 (EPSRC grant no. EP/M028267/1), the European Social Fund (ESF) through the European  
582 Union's Convergence programme administered by the Welsh Government.

583



584 **7. Bibliography**

585

- 586 1. Huang, X., et al., *Topology optimization of microstructures of cellular materials and*  
587 *composites for macrostructures*. Computational Materials Science, 2013. **67**: p. 397-  
588 407.
- 589 2. Coelho, P.G., et al., *A hierarchical model for concurrent material and topology*  
590 *optimisation of three-dimensional structures*. Structural and Multidisciplinary  
591 Optimization, 2008. **35**(2): p. 107-115.
- 592 3. Brackets, D., I. Ashcroft, and R. Hague. *Topology optimization for additive*  
593 *manufacturing*. in *Proceedings of the solid freeform fabrication symposium, Austin,*  
594 *TX*. 2011. S.
- 595 4. Leary, M., et al., *Optimal topology for additive manufacture: a method for enabling*  
596 *additive manufacture of support-free optimal structures*. Materials & Design, 2014.  
597 **63**: p. 678-690.
- 598 5. Mullins, L., *Softening of Rubber by Deformation*. Rubber Chemistry and Technology,  
599 1969. **42**(1): p. 339-362.
- 600 6. Mower, T.M. and M.J. Long, *Mechanical behavior of additive manufactured, powder-*  
601 *bed laser-fused materials*. Materials Science and Engineering: A, 2016. **651**: p. 198-  
602 213.
- 603 7. Gorsse, S., et al., *Additive manufacturing of metals: a brief review of the*  
604 *characteristic microstructures and properties of steels, Ti-6Al-4V and high-entropy*  
605 *alloys*. Science and Technology of Advanced Materials, 2017. **18**(1): p. 584-610.
- 606 8. Wadley, H.N.G., N.A. Fleck, and A.G. Evans, *Fabrication and structural performance*  
607 *of periodic cellular metal sandwich structures*. Composites Science and Technology,  
608 2003. **63**(16): p. 2331-2343.

- 609 9. Ajdari, A., H. Nayeb-Hashemi, and A. Vaziri, *Dynamic crushing and energy*  
610 *absorption of regular, irregular and functionally graded cellular structures.*  
611 *International Journal of Solids and Structures*, 2011. **48**(3-4): p. 506-516.
- 612 10. Day, J. and K. Miller, *Equibiaxial Stretching of Elastomeric Sheets, An Analytical*  
613 *Verification of an Experimental Technique*, in *ABAQUS users' conference*. 2000:  
614 Newport, RI. p. 205-220.
- 615 11. Ninjatek, *NinjaFlex® 3D Printing Filament*, in *Ninjatek Technical Specifications*,  
616 Ninjatek, Editor. 2016, Ninjatek.
- 617 12. Abueidda, D.W., et al., *Mechanical properties of 3D printed polymeric cellular*  
618 *materials with triply periodic minimal surface architectures.* *Materials & Design*, 2017.  
619 **122**: p. 255-267.
- 620 13. BSI, *BS ISO 37:2017 - Rubber, vulcanized or thermoplastic — Determination of*  
621 *tensile stress-strain properties.* 2017, BSI.
- 622 14. Treloar, L.R.G., *The physics of rubber elasticity.* 1975: Oxford University Press, USA.
- 623 15. Bergstrom, J.S., *Mechanics of solid polymers: theory and computational modeling.*  
624 2015: William Andrew.
- 625 16. Dadbakhsh, S., et al. *Effect of powder size and shape on the SLS processability and*  
626 *mechanical properties of a TPU elastomer.* in *Physics Procedia*. 2016. Elsevier.
- 627 17. Frazier, W.E., *Metal Additive Manufacturing: A Review.* *Journal of Materials*  
628 *Engineering and Performance*, 2014. **23**(6): p. 1917-1928.
- 629 18. Soe, S.P., et al., *Mechanical characterisation of Duraform® Flex for FEA hyperelastic*  
630 *material modelling.* *Polymer Testing*, 2014. **34**: p. 103-112.
- 631 19. Ahn, S.-H., et al., *Anisotropic material properties of fused deposition modeling ABS.*  
632 *Rapid prototyping journal*, 2002. **8**(4): p. 248-257.

633